Ultrasonic Imaging Techniques for Breast Cancer Detection

Nathan R. Goulding[1], Joel D. Marquez[2], Emily M. Prewett[3],
Thomas N. Claytor[4], Lianjie Huang[4], and Brett R. Nadler[4]

Nomenclature

A	Reduced amplitude of ultrasound wave due to attenuation
A_0	Amplitude of ultrasound wave at reference location
α	Attenuation coefficient
B	Bulk modulus
d	Distance in reconstruction algorithm
f	Frequency (Hz)
$image_size$	Image size in mm
L	Length of inclusion in mm
M	Matrix containing collected data
n	Number of pixels per side of reconstruction image
$nPixels$	Number of pixels in image
ϕ	Angle of migration sweep
R	Reflected energy; Radius of transducer rotation
ρ	Material density
θ	Angle of refraction or reflection; Transducer position in degrees
t	Time
V , v	Sound velocity
x_1	Transducer x-position
x_p	x-coordinate of point of interest
y_1	Transducer y-position
y_p	y-coordinate of point of interest
z	Distance wave traveled
Z	Acoustic impedance

Abstract

Improving the resolution and specificity of current ultrasonic imaging technology can enhance its relevance to detection of early-stage breast cancers. Ultrasonic evaluation of breast lesions is desirable because it is quick, inexpensive, and does not expose the patient to potentially harmful ionizing radiation. Improved image quality and resolution enables earlier detection and more accurate diagnoses of tumors, thus reducing the number of biopsies performed, increasing treatment options, and lowering mortality, morbidity, and remission percentages. In this work, a novel ultrasonic imaging reconstruction method that exploits straight-ray migration is described. This technique, commonly used in seismic imaging, accounts for scattering more accurately than standard ultrasonic approaches, thus providing superior image resolution. A breast phantom with various inclusions is imaged using a pulse-echo approach. The data are processed using the ultrasonic migration method and results are compared to standard linear ultrasound and to x-ray computed tomography (CT) scans.. For an ultrasonic frequency of 2.25 MHz, imaged inclusions and features of approximately 1mm are resolved, although better

[1] Depts. of Electrical Engineering and Computer Science, New Mexico Tech, Socorro, NM 87801
[2] Dept. of Mechanical Engineering, University of Texas – Austin, Austin, TX 78712
[3] Dept. of Mechanical Engineering, Purdue University, West Lafayette, IN 47907
[4] Los Alamos National Laboratory, Los Alamos, NM 87545

resolution is expected with minor modifications. Refinement of this application using other imaging techniques such as time-reversal mirrors (TRM), synthetic aperture focusing technique (SAFT), decomposition of the time reversal operator (DORT), and factorization methods is also briefly discussed.

Section I: Introduction

In the United States, breast cancer affects one in eight women in their lifetimes. It is the second most common and also the second most fatal cancer in women [1]. Doctors recommend that women begin regular x-ray mammography screening at the age of 40, but earlier and more frequent screening is suggested for women identified as high-risk candidates, such as those with a family history of breast or ovarian cancer. Though x-ray mammography is currently considered the gold-standard for detection of breast tumors, the technique is limited in the size of tumors that can be detected. Additionally, mammography subjects the patient to ionizing radiation, which carries inherent risks. The high false-positive rate (~80%) and a high false-negative rate (~15%) in women over the age of 40 leads to high numbers of unwarranted biopsies and excessive cases of undetected cancer. Ultrasonic imaging has the potential to replace or augment x-ray mammography as a safer, more effective breast cancer detection method.

Ultrasonic tomography is a standard imaging technique in nondestructive evaluation (NDE) and seismic research. Recently, ultrasonic imaging has gained popularity in medical diagnostic research as well, due to the availability of low cost high speed digitization hardware, signal processing and ultrasonic arrays. Ultrasonic imaging is currently utilized for a variety of medical applications including rectal cancer detection, prenatal growth assessment, bone property identification, and *in situ* tissue characterization [6-10]. A number of researchers are currently investigating tomographic ultrasonic scanners [2-5], while different algorithm techniques to improve resolution, computational efficiency associated with ultrasound imaging, etc. are also being pursued [11-16].

Due to shortcomings in the resolution and sensitivity of existing equipment and processing techniques, ultrasonic imaging is not currently in clinical use for routine breast screening. In this paper, reflection and migration imaging techniques applicable to breast tumor detection are presented. Reconstruction algorithms are described and reconstructed images of polymer cylindrical pegs are shown to validate the algorithms. An ultrasonic breast phantom with simulated inclusions is imaged and reconstructed using these techniques. Section II discusses background theory of ultrasonic waves and characteristics important to ultrasonic imaging. The experimental setup and procedure is outlined in Section III. The image reconstruction algorithm is detailed in Section IV, and the results are summarized in Section V. Section VI reviews the conclusions, and future work that can be performed in the field is introduced in Section VII.

Section II: Background

Ultrasonic imaging takes advantage of differences in the interactions of acoustic waves with tissues of varying material properties. The interactions of the waves and the tissue cells are governed by wave-propagation physics and involve the following three phenomena: the sound speed of acoustic waves, scattering, and attenuation.

The speed of an acoustic wave traveling through a material is a function of the elastic modulus and density of the material. For small displacements, the sound speed is independent of the amplitude and frequency of the acoustic wave. The velocity of acoustic wave propagation is given by

$$V = \sqrt{\frac{B}{\rho}} \tag{1}$$

where V is the speed of the acoustic wave in a given medium, B is the bulk modulus, and ρ is the material density [17]. Differences in sound speeds of different tissues result in scattering. Sound speed information, and thus material properties, can be discerned from transmitted waves.

Scattering consists of reflection, refraction, and diffraction and occurs at interfaces between materials with differing indices of refraction. When a wave enters a different material, part of the energy is reflected back into the first material and part of the wave passes into the second material undergoing a redirection and wave speed change. Diffraction, the bending of waves around the object of differing tissue, occurs when the wavelength and the object of interest are the same order of magnitude in size. The behavior of the waves depends on the angle of incidence. The material velocities for scattering are related according to Snell's law

$$\theta_1 = -\theta_1' \text{ for Reflection} \quad \text{and} \quad \frac{\sin(\theta_1)}{V_1} = \frac{\sin(\theta_2)}{V_2} \text{ for Refraction} \tag{2}$$

where V_1, V_2, are the sound speeds in each material respectively, θ_1 is the angle of incidence, θ_1' is the angle of reflection, and θ_2 is the angle of refraction [17]. Figure 1 illustrates the three modes of scattering: reflection, refraction, and diffraction.

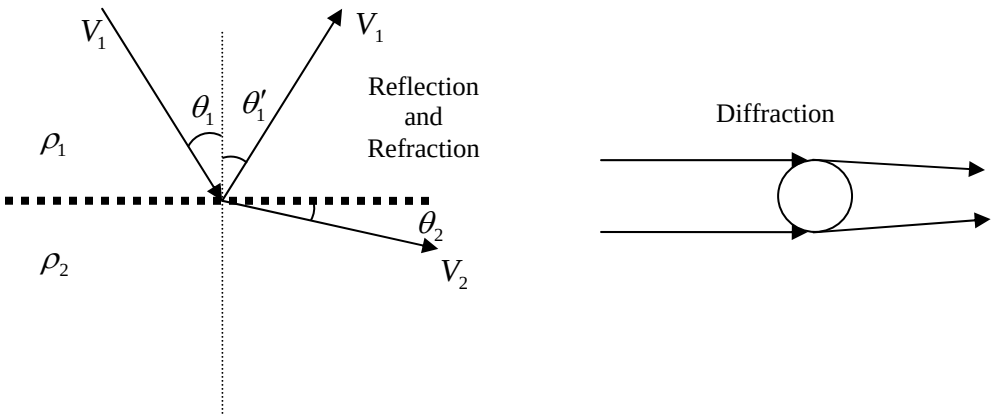

Figure 1: Illustration of three modes of scattering: reflection, refraction, and diffraction

The strength of the reflections is determined by looking at the acoustic impedance of the different materials. The acoustic impedance is given by

$$Z = \rho V \tag{3}$$

where Z is the acoustic impedance, ρ is the material density, and V is the sound speed [17]. For normal incidence, the reflected energy is given by

$$R = \left(\frac{Z_2 - Z_1}{Z_2 + Z_1} \right)^2 \tag{4}$$

where R is the reflected energy and Z_1, Z_2 are the acoustic impedance for each material respectively [17]. The scatter field provides information about boundaries and interfaces between different tissue types.

Attenuation is the loss of energy in the acoustic wave as it travels along a straight path. Attenuation is caused by scattering and absorption. Reflection, refraction, and diffraction cause energy to be deflected away from the incident direction. This energy is not lost, merely redirected. In contrast, absorption occurs when ultrasonic energy is converted into heat as it passes through a medium. This energy is not redirected and therefore is not recoverable. Attenuation, expressed as the decrease in the ultrasonic wave amplitude as it propagates through a material, is given by

$$A = A_0 \exp(-\alpha \cdot f \cdot z) \tag{5}$$

where A is the reduced amplitude, A_0 is the amplitude at a reference location, α is the attenuation coefficient, f is the frequency in Hertz, and z is the distance the wave has traveled. For human soft tissue, the value 0.5 dB/cm/MHz is commonly used for α [17].

Scattering and attenuation arise at the interfaces between different tissues within the object of interest. The effects of reflection, refraction, diffraction, and attenuation are obtained from time and spatial information in the collected waveforms. Inverse methods and algorithms are required to recover the location of the different tissue boundaries and to quantify the different material properties of these tissues.

Section III: Experimental Setup

The ultrasonic experiment setup utilizes a number of components for data acquisition and signal processing. The scanning equipment consists of two transducers driven with independent stepper motors, a z-axis motor, an x-y table, and a water tank as shown in Figure 2. The x-y platform connects to a z-axis ball screw table to allow for vertical translation of two transducers. The two motion control motors mounted on opposite sides of the z-axis ball screw independently control rotary motion of each transducer.

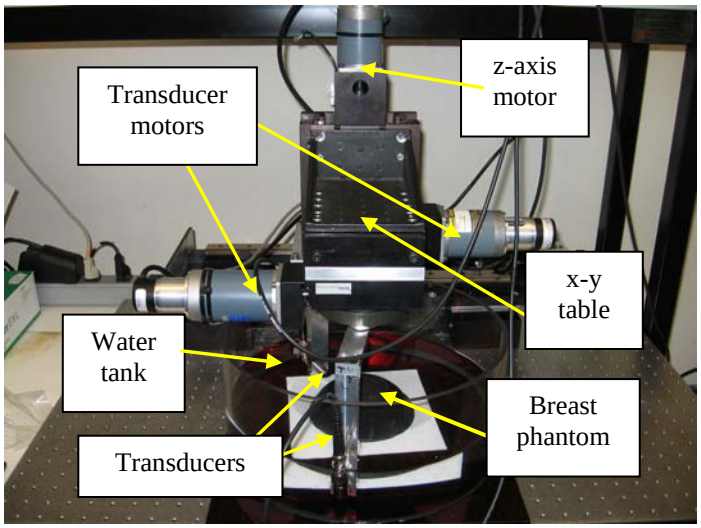

Figure 2: Equipment setup with breast phantom oriented in the center of the water tank

The transducers can be used in two modes: pulse-echo and pitch-catch. When operating in pulse-echo mode, only one transducer is used and acts as both a transmitter and receiver. In pitch-catch mode, one transducer behaves as a transmitter and emits an ultrasonic pulse, while the other transducer behaves as a receiver and collects reflections from the pulse. This arrangement effectively simulates a transducer array with an arbitrary number of elements. Using UTEX's *Winspect* Ultrasonic Data Acquisition software [18], a 20-ns negative spike excitation waveform (shown in Figure 3) is transmitted, and the signals are received and transferred to a computer for analog-to-digital conversion.

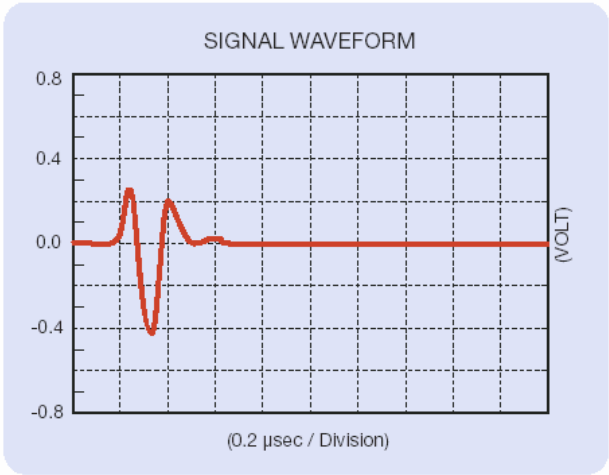

Figure 3: Transducer waveform transmission pulse: negative spike excitation

To demonstrate and quantify the beam spread of these particular transducers, a 90° scan (± 45° from axis) of a ball bearing mounted 11.4 cm from the transducer is performed. The B scan is shown in Figure 4 (a). The ball bearing is chosen because it acts as a spherical point reflector. The amplitude of the first reflection wave is extracted from the waveform data shown in Figure 4 (b) using MATLAB [19]. The data shown in Figure 4, as well as the subsequent figures, were obtained using an Acqris 310 (12 bit, 400 MHz) digitizing board operating at a 300MHz. The resulting high resolution data was subsequently downsampled in time (using Matlab) to match the physical resolution of the images as described later.

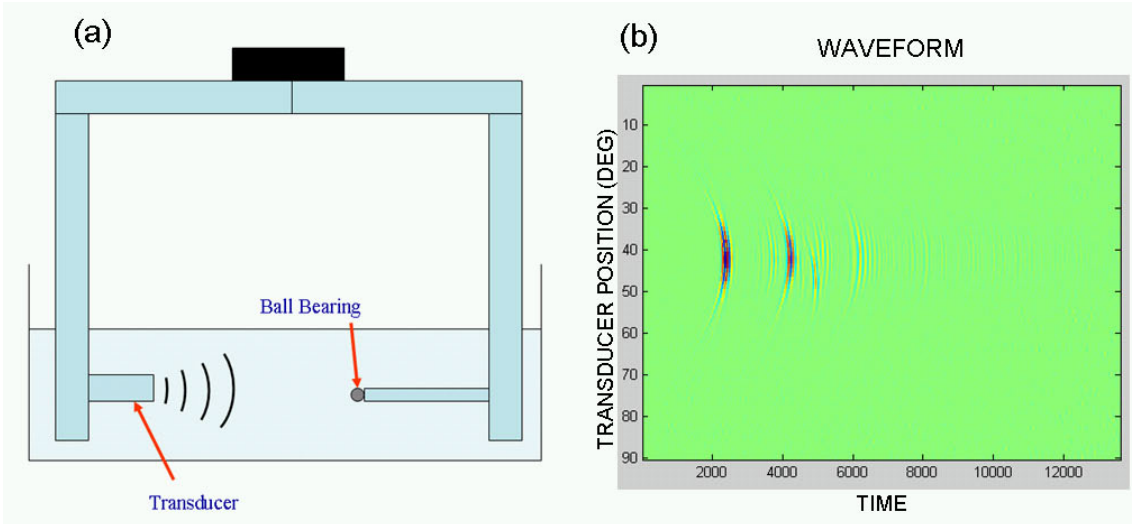

Figure 4: (a) Schematic of beam profile setup and (b) the received waveform

Thresholds are placed where the signal strength in the beam profile is 11 times weaker than at the peak, as shown in Figure 5. The signal is almost 11 times weaker at these thresholds than at its peak. Threshold locations of 28° and 58° gives a beam spread of $\pm$15° from the transducer, at a distance of 11.4 cm. The beam profile characterization verifies that critical data are not lost because of too small of a field of view. It also allows the field of view to be optimized to decrease the data set file size without losing significant data, which allows the reconstruction program to produce arcs of a smaller size. For example, sweeping across a beam width of 30° compared with 180° decreases computation time by a factor of six. A beam profile was also generated using the *Imagine3D Ultrasonic Transducer Simulation software package*; the simulated beam pattern is shown in Figure 6.

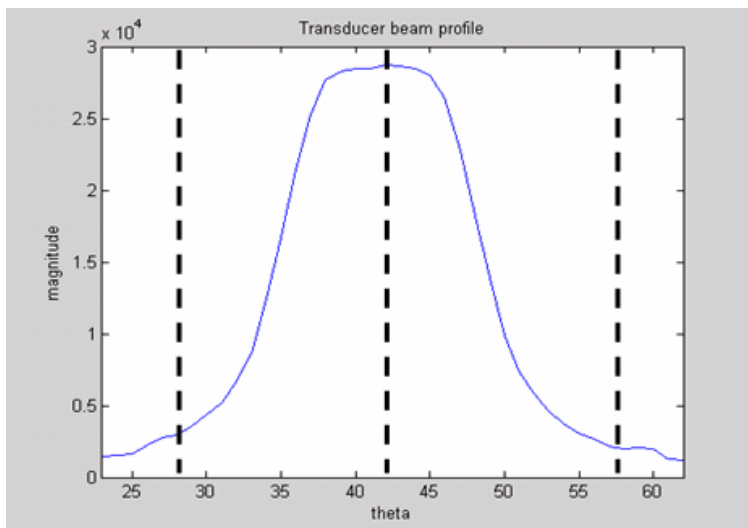

Figure 5: Transducer beam profile

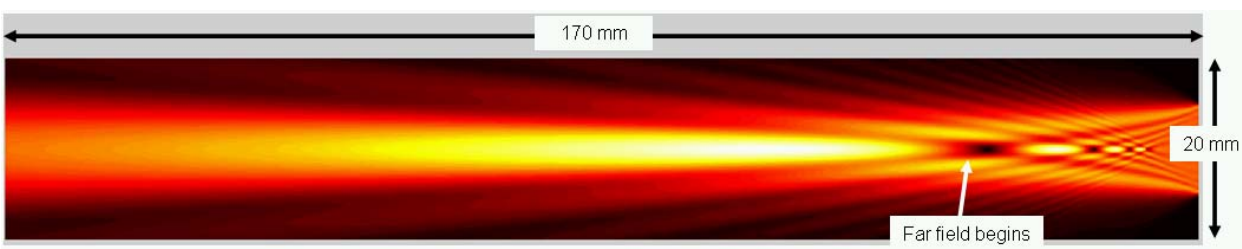

Figure 6: Simulated transducer beam profile generated using *Imagine3D* and MATLAB. Transducer is located on the right side of the image and transmits right to left.

The target to be imaged is submerged in a tank of de-ionized water and positioned in the center of the tank. The water is used for two reasons: the acoustic impedance of the water couples with the impedance of the object to reduce the amount of reflection at the front surface of the object of interest, and there is much less attenuation of the ultrasonic signal in water compared to air. Two test objects are used for imaging: a polymer cylinder 6.35 mm in diameter and a breast phantom, shown in Figure 7 (a) and (b), respectively. The phantom is a Gammex RMI 429 ultrasonic biopsy phantom [19] with various inclusions of differing size and density.

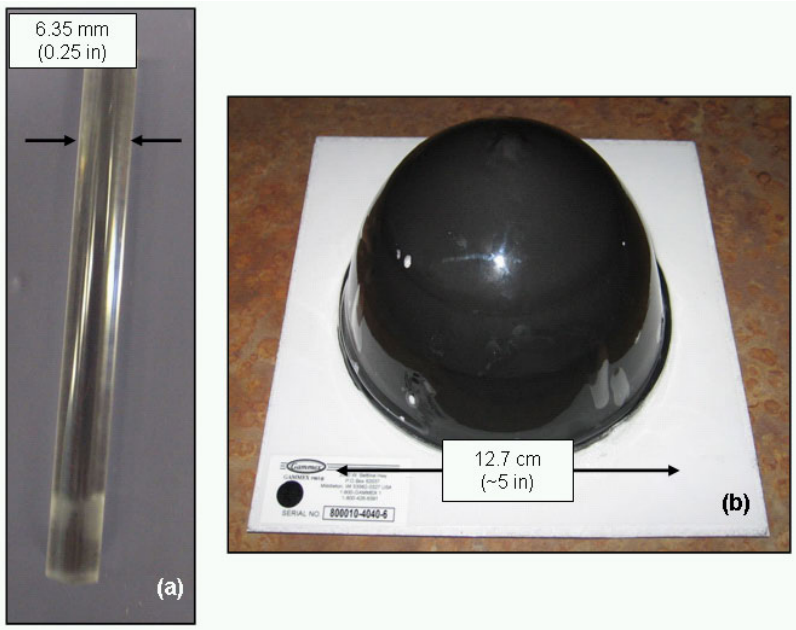

Figure 7: Image targets: (a) polymer peg, 6.35 mm diameter (b) Gammex RMI 429 phantom

The scans are performed in pulse-echo mode as shown in Figure 8. The transducer rotates 360° around the image target. The transducer transmits and receives a pulse every 1 degree. For this preliminary study, pulse-echo mode was used for convenience. Pitch-catch mode could be used and would generate much more data than pulse-echo mode, resulting in more detailed images.

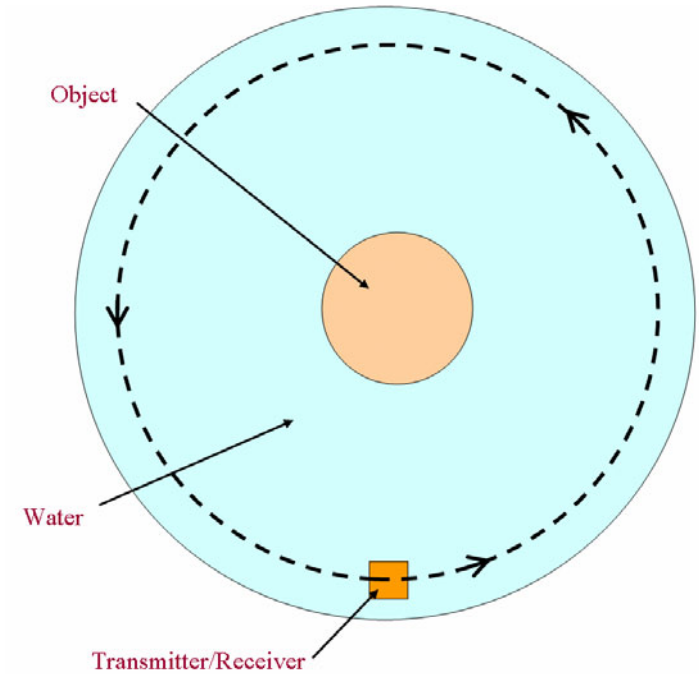

Figure 8: Scan sequence: transducer scans 360° in pulse-echo mode

Section IV: Reconstruction Algorithm

The image reconstructions are generated using straight-ray migration, homogeneous velocity, approximation methods. The image reconstruction algorithm uses collected data to recreate a representation of the image target. The process begins with a large waveform matrix, M, consisting of 360 rows and a number of columns that corresponds to the sampling rate and the data collection window. Each row corresponds to a transducer position, θ, from 1° to 360° in 1-degree increments. Along each row, the amplitude of the received waveform is stored for increasing values of time. The system uses a sampling rate of 300 MHz, so that every 300 data points correspond to 1 μs in time. To reduce computation time, the data are reduced by a factor of 20.

At each transducer angle θ, the algorithm computes the x- and y-coordinates of the location of the transducer, (x_1, y_1), as shown in the schematic in Figure 9.

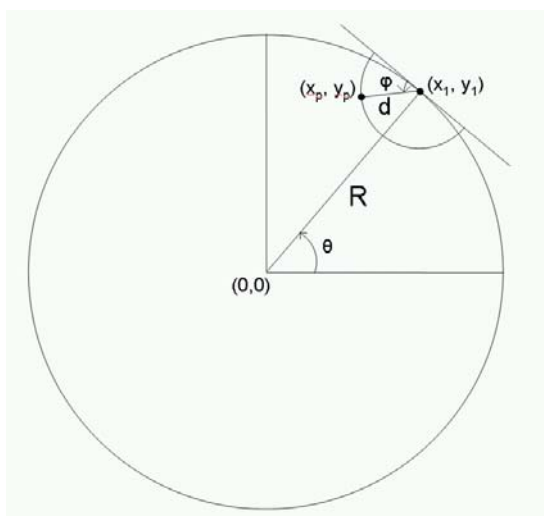

Figure 9: Geometry of migration algorithm

For a given point (x_1, y_1), the algorithm computes a distance *d* for each data point in M by converting from the time domain to the spatial domain using

$$d = t \cdot v / 2 \tag{6}$$

where *d* is the distance from (x_1, y_1) to (x_p, y_p), t is the time, and v is a fixed speed for sound in water (1500 m/s). Finally, for each distance *d*, the system computes an arc of radius *d* with origin at (x_1, y_1) between angles $75 \leq \phi \leq 105$. The angles for ϕ are chosen based upon the transducer's beam width of approximately 30°. At each point along the arc, the current waveform amplitude, M(θ, *t*), is added to the reconstruction image at coordinate (x_p, y_p).

The equations for x_1, y_1, x_p, and y_p are as follows:

$$x_1 = R\cos(\theta) \tag{7}$$

$$y_1 = R\sin(\theta) \tag{8}$$

$$x_p = x_1 - d\sin(\theta + \phi) \tag{9}$$

$$y_p = y_1 + d\cos(\theta + \phi) \tag{10}$$

where all variables are defined as in the schematic shown in Figure 9. Accumulating the amplitudes along each arc for each data (time) point and transducer angle produces an image of the scanned object. This image reconstruction algorithm does not yet weight the beam profile as shown in Figure 4 or correct for attenuation and beam spreading. Because of the circular geometry and the fact that a complete view of the object can be seen, this differs from classical seismic migration where some views are unobtainable and therefore our case can be considered as an "envelope or closed" migration. In addition, because the transducer diameter, in this case, is larger than the wavelength (0.66 mm) there may be corrections for transducer phase effects.

Section V: Results

The targets described in Section III are reconstructed using the algorithm discussed in Section IV. Three cases are considered: one polymer peg (centered and 5 mm off-center from the center of rotation of the transducer), two closely spaced polymer pegs, and one slice of the breast phantom.

The first test case is a reconstruction of a slice of one polymer peg (6.35 mm in diameter) in two orientations: centered in the tank and 5 mm away from the center. As seen in Figure 10, the waveform data are nearly straight for the centered case but form a sinusoid for the off-center case.

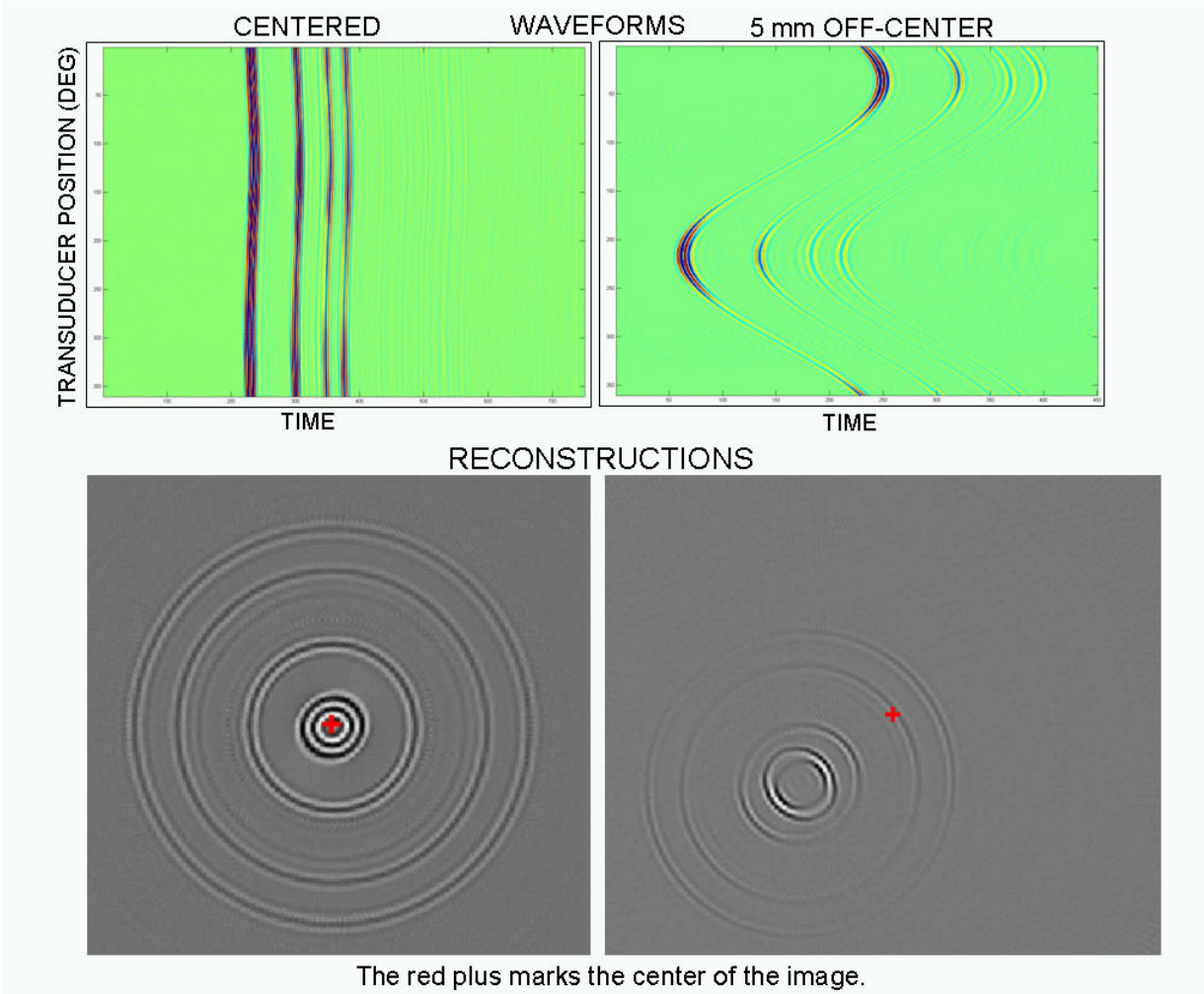

Figure 10: Waveform data and reconstructed images for one cylindrical polymer peg (a) centered and (b) 5 mm off-center from the center of rotation of the transducer

The second test case images two identical cylindrical pegs spaced 1 cm apart in the water tank. As shown in Figure 11, the algorithm reconstructs the two pegs 1.02 cm apart (2% error) and the diameter is approximately correct for both objects at 6.5 mm versus 6.3 mm. These data confirm that objects of 0.2 cm can be resolved, but further experiments are required to determine the minimum resolution. It should be noted that the data presented is a small subset (~2%) of the data that can be collected by the system for reconstruction of these images. We intend to collect a more complete data sequence using the pitch-catch technique to further enhance the images and decrease the artifacts. Other image processing techniques will also be explored to further refine these images as well. With proper selection of the reference coordinate system and the data record and sampling time, the density of data points can be adjusted to be relatively constant (~ 1-2%) over the relevant region of interest.

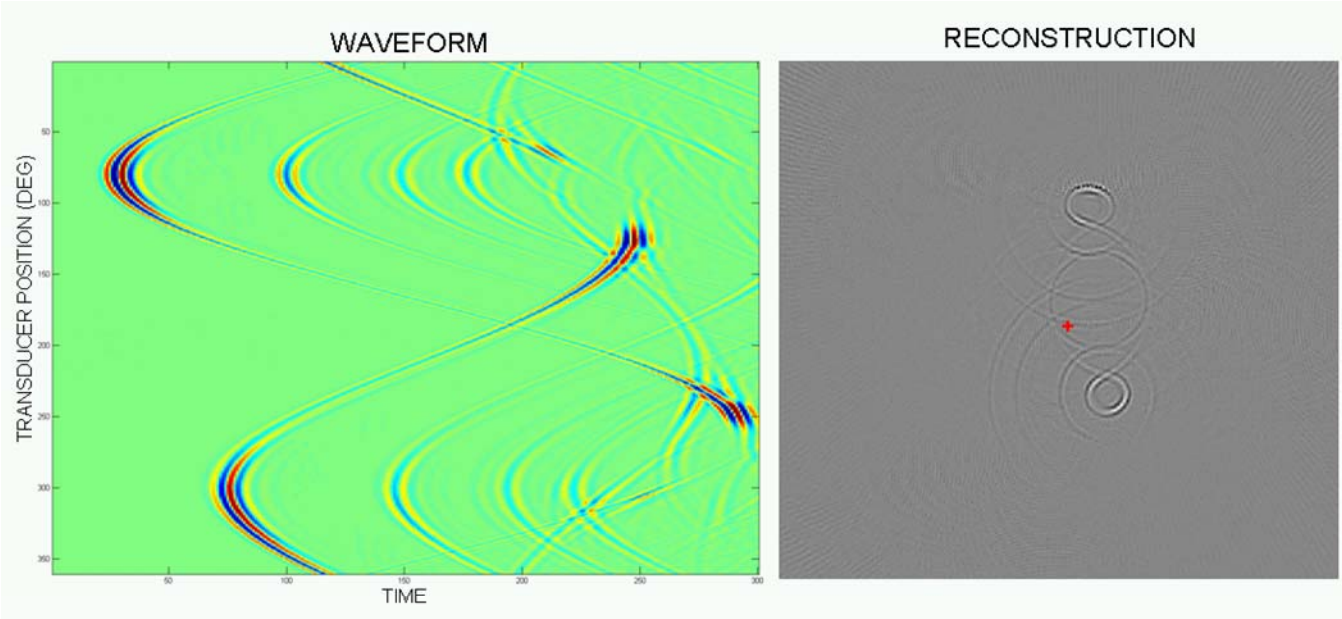

Figure 11: Waveform data and reconstructed image for two cylindrical pegs spaced 1 cm apart. The red plus in the reconstruction image represents the center of the image

The third test case images a slice of the phantom taken at approximately 20 mm measured from the top of the phantom when placed flat in the water tank. As seen in Figure 12, the reconstructed image of the phantom clearly exhibits a large inclusion.

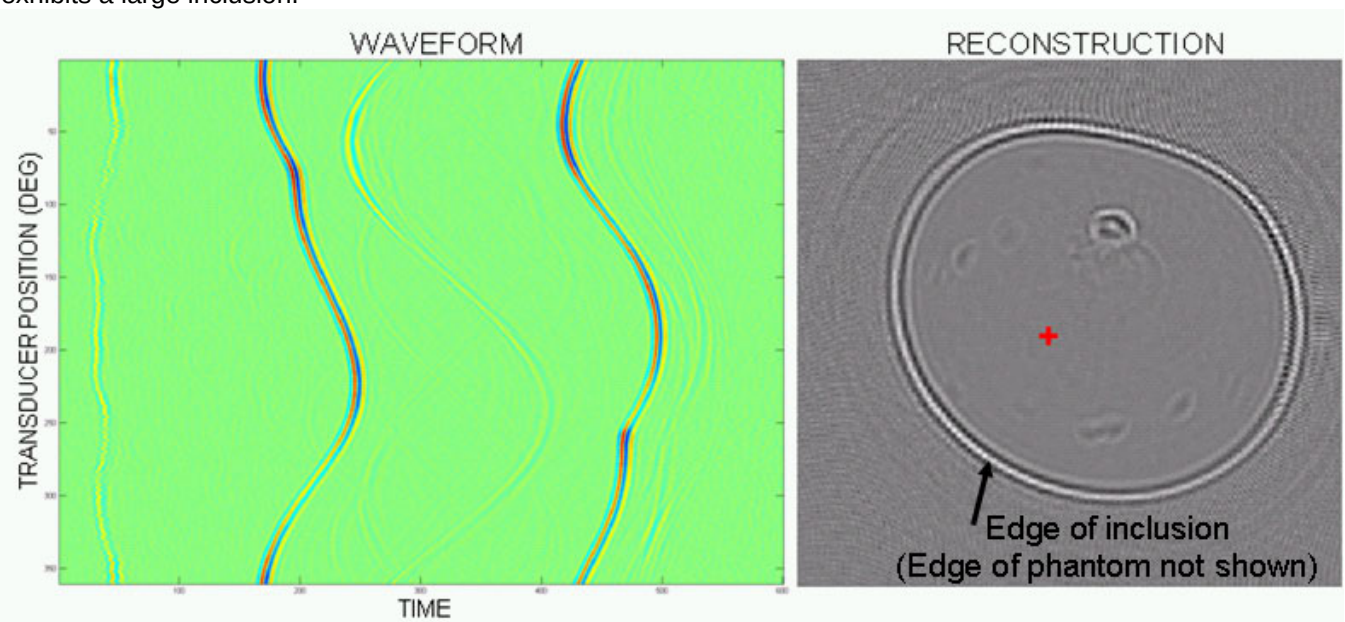

Figure 12: Waveform data and reconstructed image of 20-mm depth slice of breast phantom. The reconstructed image shows only the outline of the inclusion; the edge of the phantom is not imaged because it is acoustic impedance is coupled with that of water.

Measuring the width and height of the first inclusion in the reconstructed image yields an approximation for the physical size of the inclusion shown in Figure 13. Converting from pixels to millimeters is accomplished using

$$L = nPixels \cdot \frac{image_size}{n} \tag{11}$$

where L is the length of the inclusion (in millimeters), *nPixels* is the number of pixels measured in the image, *image_size* is the size of the image in millimeters, and *n* is the number of pixels per side of the reconstructed

image. The cross-section of the inclusion depicted in Figure 13 is an ellipse approximately 13.3 mm along the major axis and 11.9 mm along the minor axis. The size of the inclusion is in accordance with the manufacturer's specifications of the inclusion being between 10 and 15 mm in diameter.

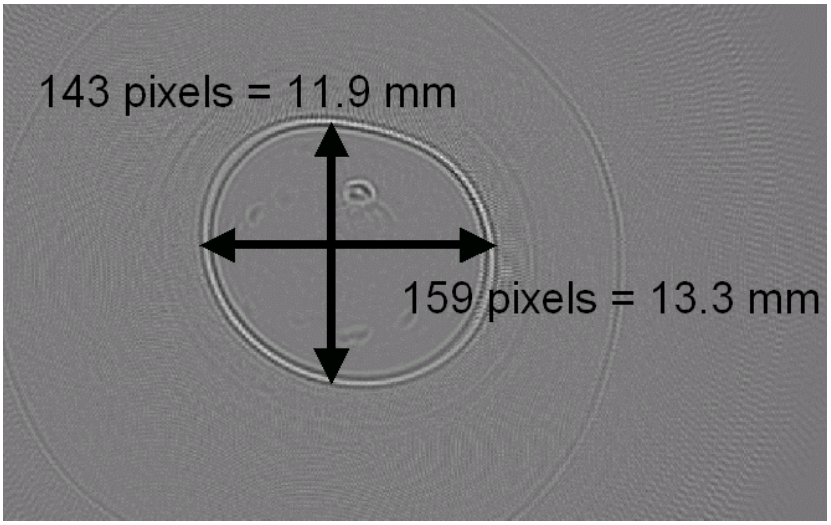

Figure 13: Reconstruction of large inclusion in phantom, with dimensions

X-ray computed tomography (CT) images were taken to compare the ultrasonic migration reconstruction to that obtained using commercially available imaging techniques. The CT cross section shown in Figure 14 was obtained with a 150 kV source operating at 80 μA for 15 minutes. This is a nominally higher voltage than used in medical CT applications. The flat panel imager (Varian 2520) produces much higher resolution images (150 micron pixels versus 500 micron pixels) than conventional medical CT. As demonstrated in Figure 14, both the reconstructed image and the CT image of the same slice of the phantom (approximately 20 mm from the top) show a large inclusion approximately 12-13 mm in size. The data sheet from the manufacturer describes the size of this inclusion as 10-15 mm. The inclusion is approximately the same size and shape in both images.

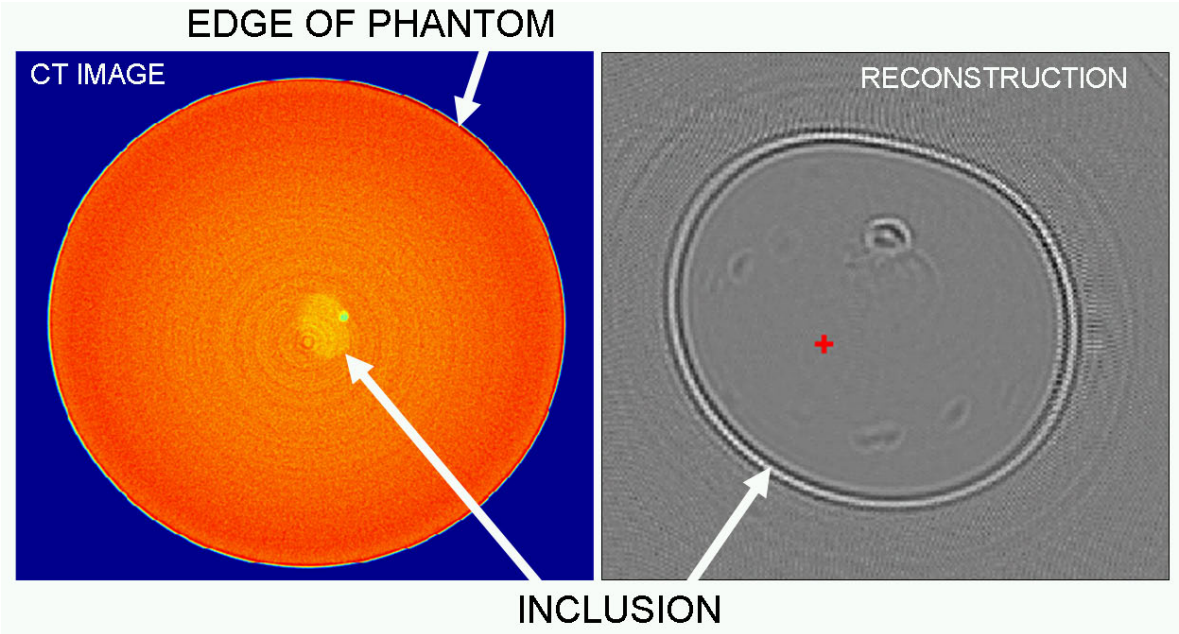

Figure 14: X-ray computed tomography (CT) image compared with the ultrasonic migration reconstruction image of the inclusion, both show a small feature that was an unintentional part of the simulated, water filled, cyst.

Section VI: Conclusions

Using a "closed" straight-ray full-waveform migration reconstruction algorithm developed in MATLAB, images of several objects have been recovered from ultrasonic data. Reconstructions of a single polymer peg, two polymer pegs, and a simulated cystic inclusion in a breast phantom have been generated. Using these images and converting from pixels to a distance using (11), the estimated sizes and shapes of the objects were computed and compared with the measured sizes. Although the algorithm produced the most accurate reconstructions when objects were centered in the tank, objects near the center were also imaged with reasonable resolution. The system resolved objects as small as 6.35 mm, separated by 10 mm. Further experiments are necessary to determine the minimum resolution of the closed migration algorithm.

Section VII: Future Work

This paper describes a preliminary reconstruction algorithm that uses reflection data to image breast tumors. The next step should apply the methods demonstrated in this paper to a two-axis scan using two transducers in pitch-catch mode. Additional reconstructed slices of the phantom could be electronically stacked together to create a 3-dimensional image of the phantom showing the size, location, and orientation of internal structures in relation to each other and the boundaries of the phantom. The experimental setup demonstrated in this paper is well suited for ultrasonic computed tomography (CT) scanning as well. Additional data sets of ultrasonic CT scans could be taken for more extensive image characterization of limiting cases. Further research should focus on refining the reconstruction algorithm using advanced methods such as synthetic aperture focusing techniques (SAFT), time-reversal mirrors (TRM), decomposition of the time-reversal operator (DORT), and factorization methods.

Acknowledgements

The authors thank Nebojsa Duric[5] for his advice regarding the experimental procedure and algorithm methods discussed in this paper. The authors also thank HYTEC Incorporated (Los Alamos, NM) for performing the 3D x-ray computed tomography scans. The financial support of the Los Alamos Dynamics Summer School, which is part of the Los Alamos National Laboratory (LANL) – University of California – San Diego Engineering Institute, and the LANL Laboratory Directed Research and Development (LDRD) program, is gratefully acknowledged. The authors also recognize The MathWorks, Inc. (Natick, MA) for their generous donation of the MATLAB software used to perform all data analysis and image reconstruction.

References

[1] American Cancer Society, http://www.cancer.org, 2006.

[2] Duric, N., Littrup, P., Babkin, A., Chambers, D., Azevedo, S., Kalinin, A., Pevzner, R., Tokarev, M., Holsapple, E., Rama, O., Duncan, R., "Development of ultrasonic tomography for breast imaging: Technical assessment." *Medical Physics*, Vol. 32 (5), 1375-1386, 2005.

[3] Jeong, J., Kim, T., Shin, D., Do, S., Singh, M., Marmarelis, V., "Soft tissue differentiation using multiband signatures of high resolution ultrasonic transmission tomography." *IEEE Transactions on Medical Imaging*, Vol 24 (3), 399-408, 2005.

[4] Lehman, C., Andre, M., Fecht, B., Johansen, J., Shelby, R., Shelby, J., "Through-transmission US applied to breast imaging." *Academic Radiology*, Vol. 7 (2), 100-107, 2000.

[5] Johnson, S., Borup, J., Wiskin, W., Natterer, F., Wuebbling, F., Zhang, Y., Olsen, C., United States Patent 6,005,916, 1999.

[6] Kim, J.C., Kim, H.C., Yu, C., Han, K., Kim, J.R., Lee, K., Jang, S., Lee, S., Ha, H., "Efficacy of 3-dimensional endorectal ultrasonography compared with conventional ultrasonography and computed tomography in preoperative rectal cancer staging." *The American Journal of Surgery*, Vol. 192, 89-97, 2006.

[7] Keenan, D., Shorter, P., "Simulation by Diffusion on a Manifold with Boundary: Applications to Ultrasonic Prenatal Medical Imaging." *SIAM Journal of Applied Mathematics*, Vol. 64 (3), 932-960, 2004.

[8] Hoffmeister, B., AUwarter, J., Rho, J., "Effect of marrow on the high frequency ultrasonic properties of cancellous bone." *Physics in Medicine and Biology*, Vol. 47, 3419-3427, 2002.

[9] Jensen, M.S., Wiljelm, J.E., Sahl, B., Brandt, T., Martinsen, K., Jespersen, S.K., Falk, E., "A method to obtain reference images for evaluation of ultrasonic tissue characterization techniques." *Ultrasonics*, Vol. 40, 89-94, 2002.

[10] Goldstein, A., Powis, R.L., "Medical ultrasonic diagnostic." Physical Acoustics, Vol. 23, 46-191, 1999.

[11] Simonetti, F., "Multiple scattering: The key to unravel the subwavelength world from the far-field pattern of a scattered wave." *Phys. Rev. E*, Vol 73 (3), 036619-1-036619-13, 2006.

[5] Karmanos Cancer Institute, Detroit, MI

[12] Lavarello, R., Kamalabadi, F., O'Brien, W.D. Jr., "A Regularized Inverse Approach to Ultrasonic Pulse-Echo Imaging." *IEEE Transactions on Medical Imaging*, Vol. 25 (6), 712-722, 2006.
[13] Cui, J., He, J., "2D seismic migration with compensation: a preliminary study." *Journal of Geophysics and Engineering*, Vol. 1, 263-267, 2004.
[14] Huang, L., Duric, N., Littrup, P., "Ultrasonic breast imaging using a wave-equation migration method." *Proceedings of SPIE, Medical Imaging 2003: Ultrasonic Imaging and Signal Processing*, Vol. 5035, 432-439, 2003.
[15] Lukin, V., Ponomarenko, N., Abramov, S., Egiazarian, K., Astola, J., "Automated Robust Procedure for SAR Image Filtering and Preliminary Analysis." *Proceedings of SPIE*, Vol. 4883, 48-59, 2003.
[16] Kerbrat, E., Prada, C., Cassereau, D., Fink, M., "Ultrasonic Nondestructive Testing of Scattering Media Using the Decomposition of the Time-Reversal Operator." *IEEE Transactions on Ultrasonics, Ferroelectrics, and Frequency Control*, Vol. 49 (8), 1103-1113, 2002.
[17] Bushberg, J.T., Seibert, J.A., Leidholdt, E.M. Jr., Boone, J.M., *The Essential Physics of Medical Imaging*, 2nd Edition, Philadelphia: Lippincott Willams and Wilkins, 469-553, 2001.
[18] Winspect Non Destructive Inspection Software User Manual, Release 6.0, UTEX Scientific Instruments, Inc., 2004.
[19] Documentation for Mathworks Products, R2006a, The Mathworks, Inc., 2006.
[20] Ultrasound Biopsy Phantom RMI: A User's Guide, Gammex RMI, 1996.